Supporting Information

In-Situ Grown Na^+-Doped $NH_4V_4O_{10}$ Nano-Arrays on Carbon Cloth with Ultra-High Specific Capacity for High-Performance Aqueous Ammonium Ion Hybrid Supercapacitors

Yangwang Zhou[a,b], Fei Long[b], Yixin Hou[b], Xinying Lin[a,b], Li Sun[b], Shuyi Mo[a], Fei Long[a,*], Yihua Gao[a,b,*]

[a] School of Materials Science and Engineering, Guangxi Key Laboratory of Optical and Electronic Materials and Devices & Collaborative Innovation Center for Exploration of Nonferrous Metal Deposits and Efficient Utilization of Resources, Guilin University of Technology (GUT), Guilin 541004, China

[b] Center for Nanoscale Characterization & Devices (CNCD), School of Physics & Wuhan National Laboratory for Optoelectronics (WNLO), Huazhong University of Science and Technology (HUST), Wuhan 430074, China

* Corresponding authors.

E-mail: longf@glut.edu.cn (F. L.); gaoyihua@hust.edu.cn (Y. G.)

Experiments Section

1. Reagents and materials

Ammonium metavanadate (NH_4VO_3) were supplied by Aladdin. Oxalic acid dihydrate ($H_2C_2O_4·2H_2O$), Sodium chloride (NaCl), Hydrochloric acid (HCl) and Ammonium sulfate ($(NH_4)_2SO_4$) were purchased from Sinopharm Chemical Reagent Co., Ltd. Lithium fluoride (LiF, 99%) was purchased from Macklin Inc. Ti_3AlC_2 powder was purchased from Foshan Xinxi Technology Co., Ltd. All chemicals were used as received without any further purification. Carbon cloth (CC) was purchased from Suzhou Zhengtairong New Material Co., Ltd.

2. Synthesis of NaNVO@CC and NVO@CC cathode

The carbon cloth (CC) was cleaned with HCl, acetone, absolute ethanol, and deionized (DI) water, respectively. 3.75 mmol of NH_4VO_3 and 4.5 mmol of $H_2C_2O_4·2H_2O$ were mixed in to 75 ml of deionized water and stirred for 40 min. A light yellow transparent solution was obtained. Then 1.88 mmol of NaCl was added to the above solution and stirred for another 10 min to dissolve them completely. The mixed solution was transferred to a Teflon-lined autoclave (100 mL) and the clean CC (2 cm × 3 cm) was added, and kept at 180 ℃ for 8 h. After the reaction， the carbon cloth was rinsed by ethanol and DI water three times and subsequently dried at 60 ℃ for 12 h to obtain NaNVO@CC. For comparison, the preparation material without added NaCl was marked as NVO@CC. The mass loading of active materials grown on the CC was about 0.8 mg cm^{-2}.

3. Synthesis of $Ti_3C_2T_x$ MXene anode

According to literature reports, the layer $Ti_3C_2T_x$ MXene nanosheets were prepared by etching aluminum from Ti_3AlC_2 in HCl and LiF mixed solution. To put it simply, 1.0 g LiF was gently added to 20.0 mL HCl (9.0 M) and kept magnetic stirring until completely dissolved. Then, 1.0 g Ti_3AlC_2 was added to the above solution stably, stirred at the temperature of 35 ℃ for 24.0 h. After complete reaction, the mixture was centrifuged at 3500 rpm for 5.0 min again and again until the pH value reached about 6. After centrifugation, the sediment was redispersed in deionized water and ultrasonic processed for 1.0 h under certain condition (Ar atmosphere and below 35 ℃). Last, the

above solution was centrifuged at 3500 rpm for 30.0 min again to obtain the supernatant of layer $Ti_3C_2T_x$ MXene nanosheets. The $Ti_3C_2T_x$ MXene film was obtained through vacuum filtration. The specific steps were as follows: Firstly, the supernatant of the prepared 8 mL of 5 mg mL^{-1} $Ti_3C_2T_x$ MXene nanosheets was vacuum filtered through a water-based filter membrane with a diameter of 50 mm and a pore size of 220 nm. Subsequently, the filtered solution was placed in an oven at 40 °C for drying. After this process, the final product was a $Ti_3C_2T_x$ MXene thin film.

4. Materials characterization

The morphology and microstructure of the products were characterized using scanning electron microscopy (SEM, FEI Nova NanoSEM 450). The structure and phase purity of the as-synthesized products were revealed by X-ray diffraction (XRD, Rigaku X-ray diffractometer with Cu Kα radiation). X-ray photoelectron spectrometry (XPS) analysis was carried out on a Thermofisher Nexsa spectrometer with Al Kα radiation for excitation. FTIR measurements were carried out on a Thermo Scientfic Nicolet iS20. Raman spectroscopy was performed on a laser confocal spectrometer (LabRAM HR800). Electron paramagnetic resonance (EPR) measurements were performed on Bruker EMXplus-6/1. Thermogravimetry analysis (TGA) (Pyris1 TGA) was performed under air atmosphere from 25 ℃ temperature to 500 ℃ at a heating rate of 10 ℃ min^{-1}.

5. Electrochemical measurements

The electrochemical performance of the single electrode was explored in a three-electrode system with working electrode (active materials: acetylene black: PVDF= 8.00:1.00:1.00), reference electrode (Ag/AgCl), counter electrode (carbon rod), and electrolyte (1.00 M $(NH_4)_2SO_4$). The mass loading of active materials on the Ti collector was about 1.0 mg cm^{-2}.

The NaNVO@CC//$Ti_3C_2T_x$ MXene A-HSC was tested in a two-electrode system. The electrochemical performances of electrodes and the A-HSC including cyclic voltammetry (CV) and electrochemical impedance spectroscopy (EIS) were tested using the electrochemical workstation (CHI660E). Galvanostatic charge-discharge (GCD) and the cycle life measurements were performed on a LAND-CT2001A battery

workstation.

6. Computational Details.

The specific capacity (Q) and specific capacitance (C) are respectively calculated from equations (1) and (2).

$$Q = \frac{I \times \Delta t}{m} \tag{1}$$

$$C = \frac{I \times \Delta t}{m \times \Delta U} \tag{2}$$

Where I (A) is the discharge current, Δt (s) is the discharge time of galvanostatic charge-discharge, m (g) is the mass of electroactive material, and ΔU (V) is the potential window.

As the GCD curves of the devices are approximately linear, the energy density (E, Wh kg^{-1}) and power density (P, W kg^{-1}) of A-HSC are determined by equation (3) and equation (4), respectively.

$$E = 0.5 \times \frac{C \times \Delta U^2}{3600} \times 1000 \tag{3}$$

$$P = \frac{3600E}{\Delta t} \tag{4}$$

Where the specific capacitance (C) can be obtained through equation (2), Δt is the discharge time.

The capacitance retention (CR) and coulomb efficiency (CE) are respectively calculated from equations (5) and (6).

$$CR = \frac{\Delta t}{\Delta t_0} \tag{5}$$

$$CE = \frac{\Delta t_d}{\Delta t_c} \tag{6}$$

Where Δt is the discharge time of different cycles and Δt_0 is the initial discharge time, and Δt_d is the discharge time and Δt_c is the charge time in same cycle.

Table S1. Comparison of the ionic radius, hydrated ionic radius, and ionic weight of different carriers.

Ionic	NH_4^+	Li^+	Na^+	K^+	Zn^{2+}	Ca^{2+}	Mg^{2+}	Al^{3+}
Ionic Radius (Å)	1.48	0.6	0.95	1.33	0.74	0.99	0.65	0.5
Hydrated Radius (Å)	3.31	3.82	3.58	3.31	4.30	4.12	4.28	4.75
Ionic Weight (g mol^{-1})	18	6	23	39	65	40	24	27

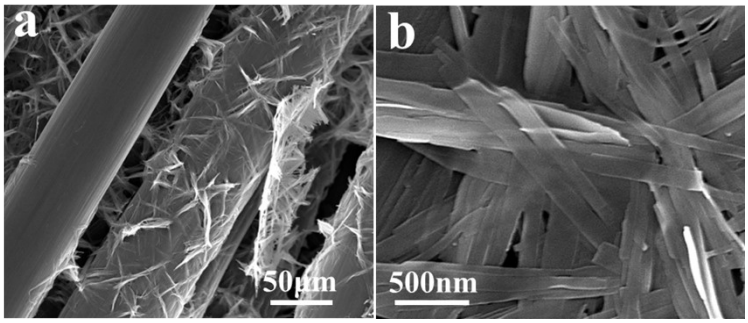

Fig. S1. SEM images of NVO@CC at different magnifications.

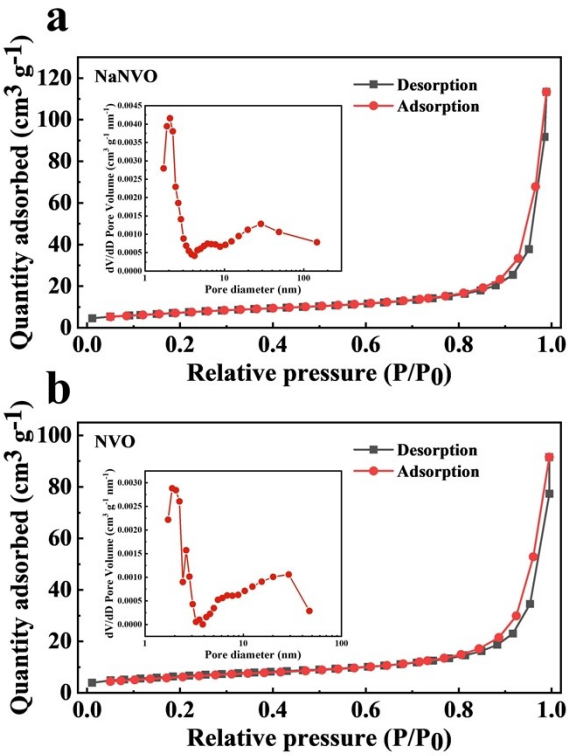

Fig. S2. Nitrogen adsorption-desorption isotherms and the corresponding pore size distribution curves for two samples. (a) NaNVO and (b) NVO.

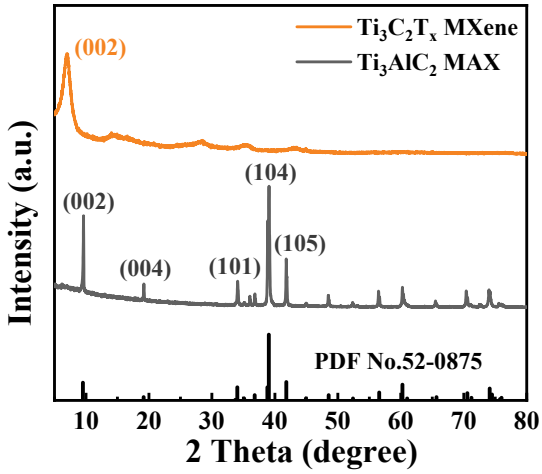

Fig. S3. The XRD patterns of Ti_3AlC_2 MAX powder and $Ti_3C_2T_x$ MXene powder.

Fig. S3 shows the XRD patterns of the MXene and MAX. After etching Al from MAX, the mainly typical peaks of MAX disappear and a new peak of around 7° appears, which means the successful preparation of $Ti_3C_2T_x$ MXene.

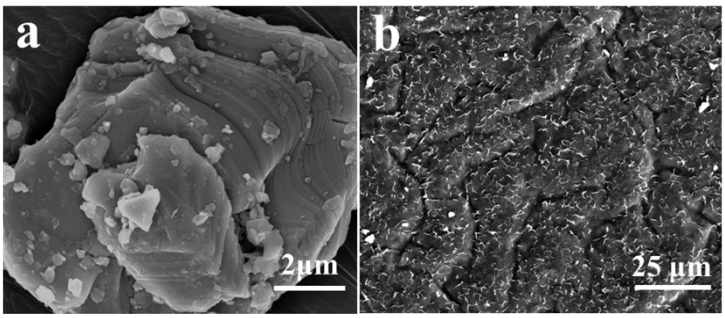

Fig. S4. SEM images of (a) Ti_3AlC_2 MAX powder and (b) $Ti_3C_2T_x$ MXene anode.

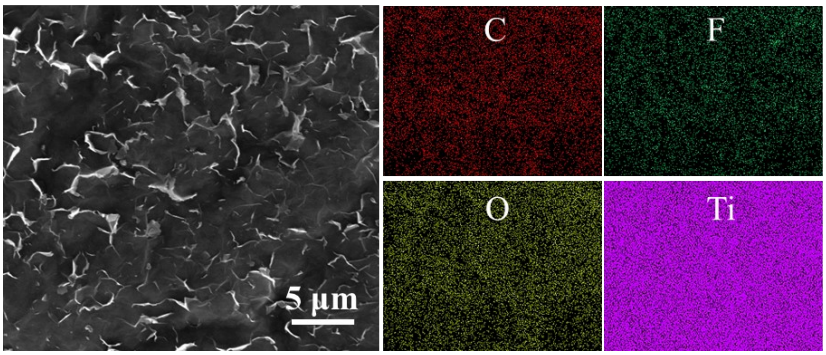

Fig. S5. The SEM images and EDS mappings of $Ti_3C_2T_x$ MXene anode.

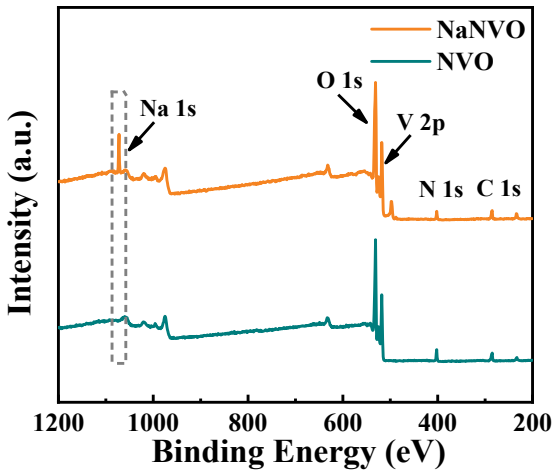

Fig. S6. Survey XPS spectra of NVO and NaNVO samples.

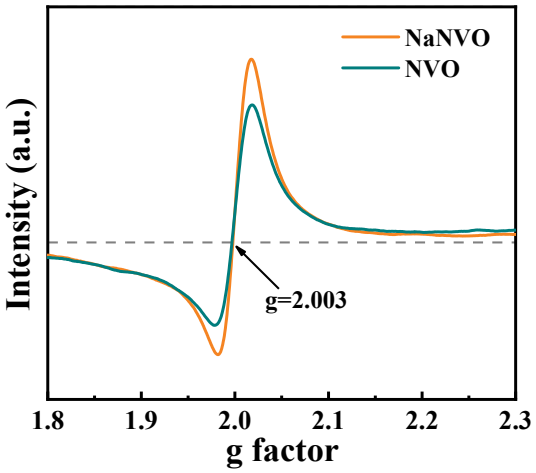

Fig. S7. EPR spectra of NVO and NaNVO.

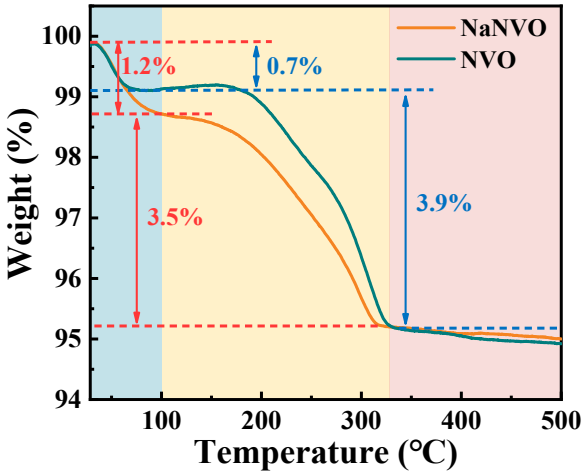

Fig. S8. TG curves of NVO and NaNVO samples.

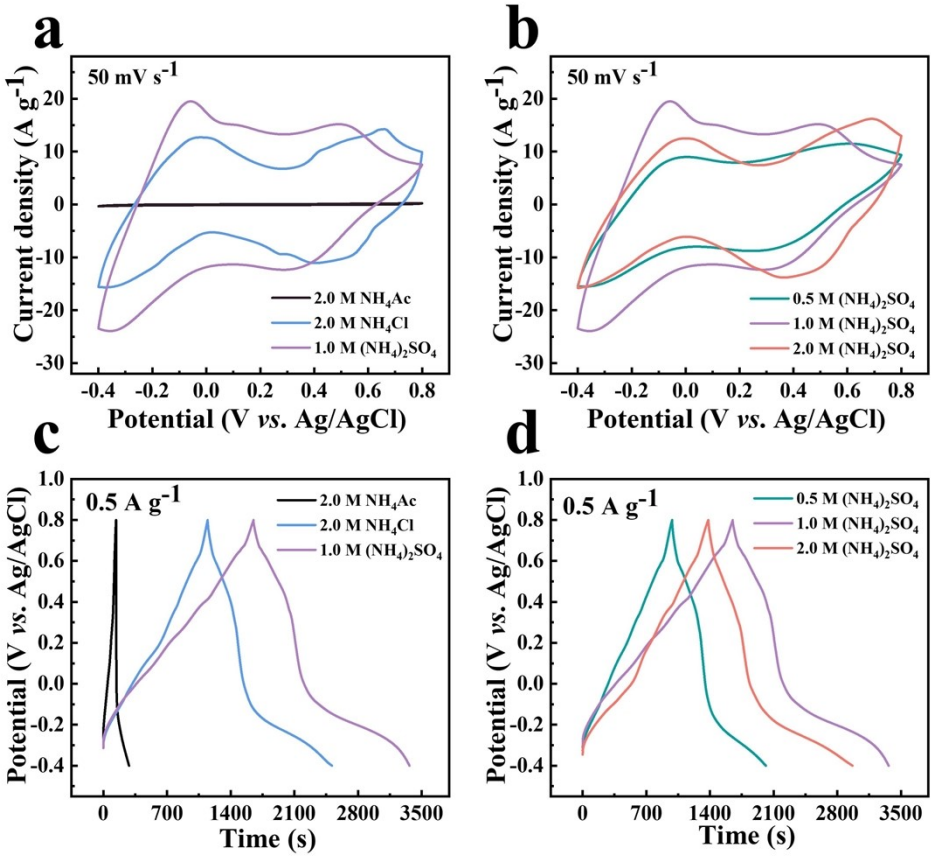

Fig. S9. (a) CV curves of NaNVO@CC in 2.0 M NH_4^+ electrolytes at 50.0 mV s^{-1}. (b) CV curves of NaNVO@CC in different concentrations of $(NH_4)_2SO_4$ electrolytes at 50.0 mV s^{-1}. (c) GCD curves of NaNVO@CC in 2.0 M NH_4^+ electrolytes at 0.50 A g^{-1}. (d) GCD curves of NaNVO@CC in different concentrations of $(NH_4)_2SO_4$ electrolytes at 0.50 A g^{-1}.

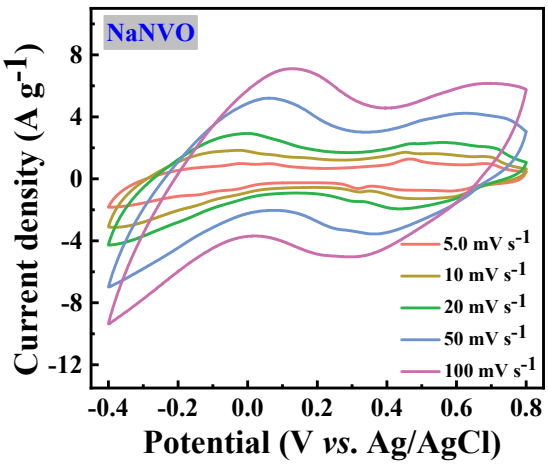

Fig. S10. CV curves of NaNVO from 5.0 mV s^{-1} to 100 mV s^{-1}.

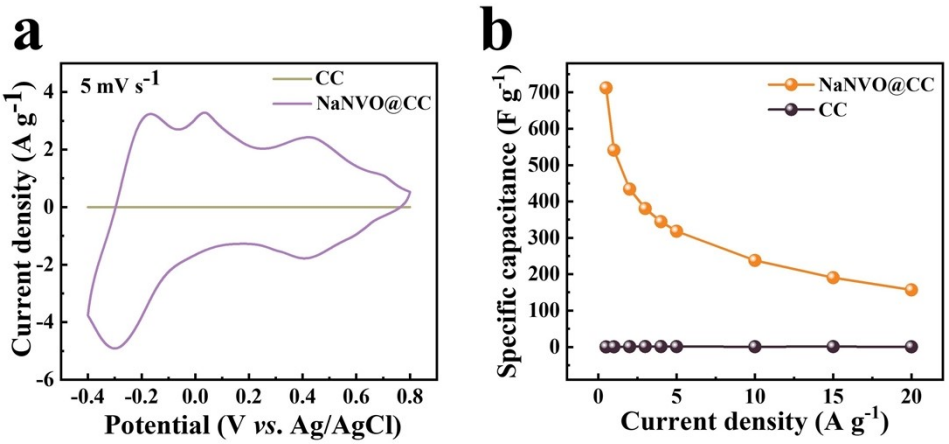

Fig. S11. (a) CV curves of NaNVO@CC and carbon cloth at a scan rate of 5.0 mV s^{-1}. (b) Specific capacitances of NaNVO@CC and carbon cloth as a function of current density.

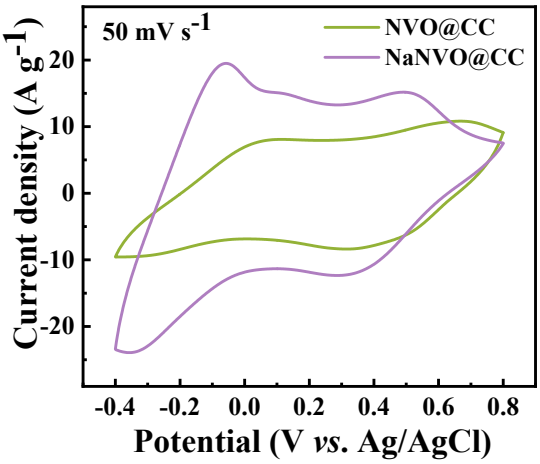

Fig. S12. CV curves of NaNVO@CC and NVO@CC at a scan rate of 50 mV s^{-1}.

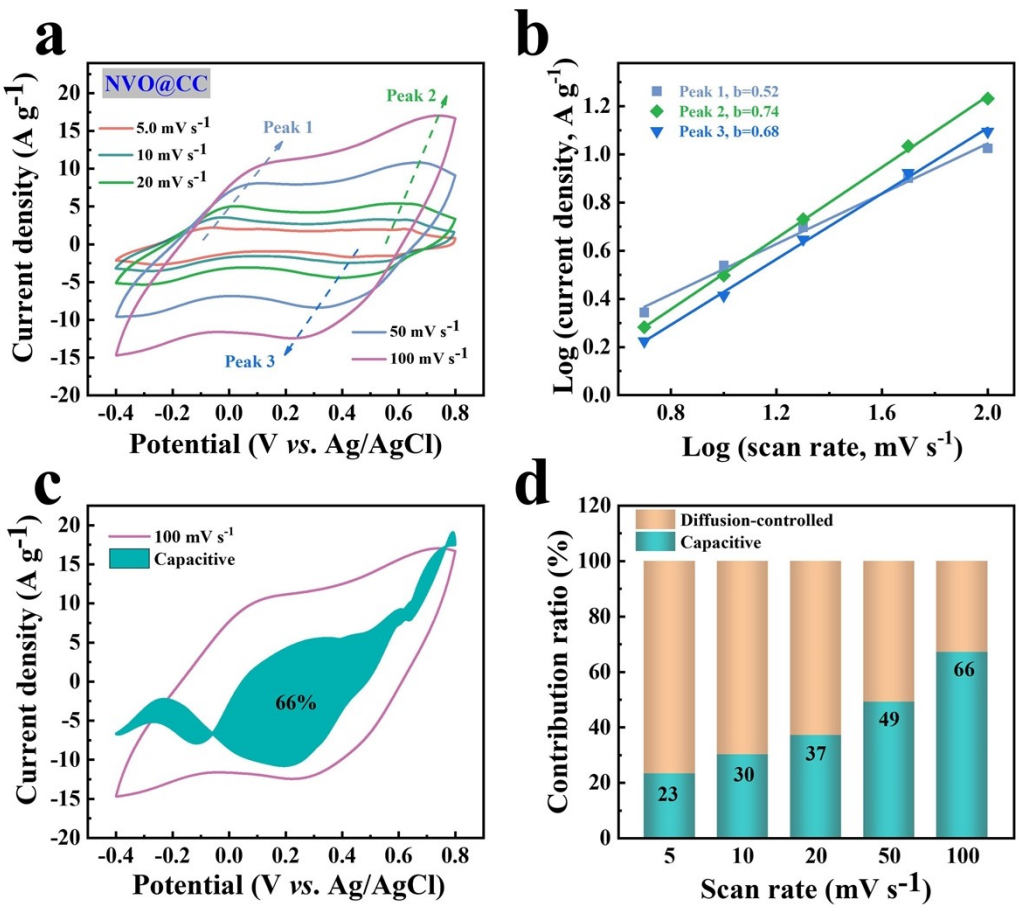

Fig. S13. (a) CV curves of NVO@CC from 5.0 mV s^{-1} to 100 mV s^{-1}. (b) log(*i*) vs. log(*v*) plots of three peaks. (c) Capacitive contribution at scan rate of 100 mV s^{-1} of NVO@CC. (d) Contribution ratios of the capacitive and diffusion-controlled at different scan rates of NVO@CC.

Material	Electrolyte	Capacitance	Current density	Cycle performance	Ref.
NaNVO@CC	1.0 M $(NH_4)_2SO_4$	712 F g^{-1}	0.5 A g^{-1}	71.1% retained after 20,000 cycles at 5 A g^{-1}	This work
PVO	1.0 M PVA/NH_4Cl	351 F g^{-1}	1 A g^{-1}	56.0% retained after 10,000 cycles at 3 A g^{-1}	1
MnHCF	1.0 M NH_4TFSI	108 F g^{-1}	0.5 A g^{-1}	—	2

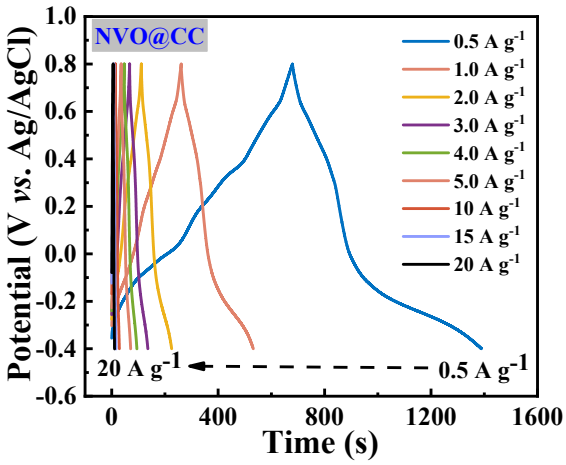

Fig. S14. GCD curves of NVO@CC from 0.50 A g^{-1} to 20 A g^{-1}.

PANI-intercalated V_2O_5	0.5 M $(NH_4)_2SO_4$	462 F g^{-1}	1 A g^{-1}	97% retained after 100 cycles at 20 A g^{-1}	3
$MnO_{x\text{-}40}$	0.5 M NH_4Ac	792 F g^{-1}	0.5 A g^{-1}	94.7% retained after 10,000 cycles at 5 A g^{-1}	4
ACC@VPP	1.0 M PVA/NH_4Cl	511 F g^{-1}	0.5 A g^{-1}	72% retained after 10,000 cycles at 0.5 A g^{-1}	5
h-MoO3	1.0 M NH_4Cl	282 F g^{-1}	1 A g^{-1}	94% retained after 100,000 cycles at 15 A g^{-1}	6
MoS2@PANI	1.0 M NH_4Cl	452 F g^{-1}	1 A g^{-1}	86.8% retained after 5,000 cycles at 20 A g^{-1}	7
$(NH_4)_{1.47}Ni[Fe(CN)_4]_{0.88}$	1.0 M $(NH_4)_2SO_4$	270 F g^{-1}	0.15 A g^{-1}	74% retained after 2,000 cycles at 0.3 A g^{-1}	8
NVO	1.0 M NH_4Cl/PVA	339 F g^{-1}	0.5 A g^{-1}	71% retained after 2,000 cycles at 100 mV s^{-1}	9

Table S2. Comparison of electrochemical properties of NaNVO@CC for NH_4^+ storage with previously reported works.

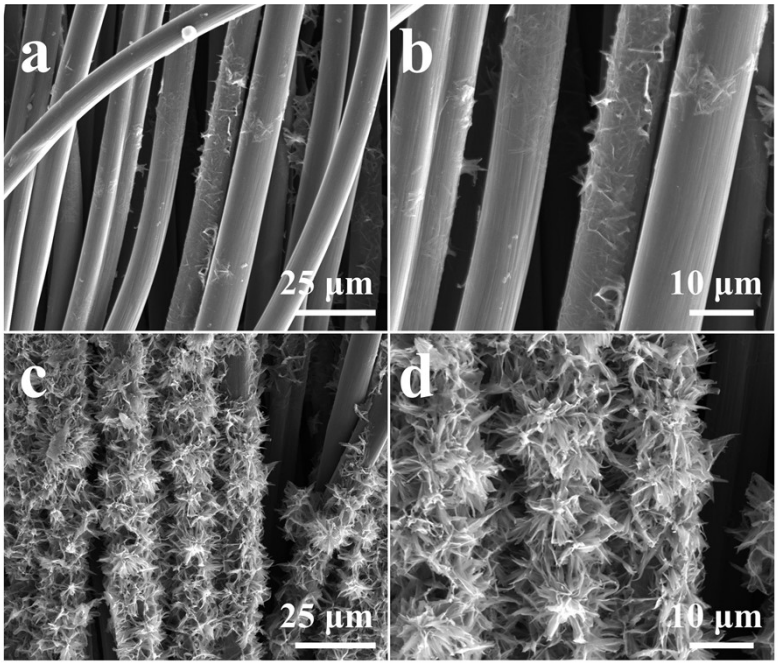

Fig. S15. SEM images of different samples after 2000 cycles at 5.0 A g^{-1}. (a, b) NVO@CC and (c, d) NaNVO@CC.

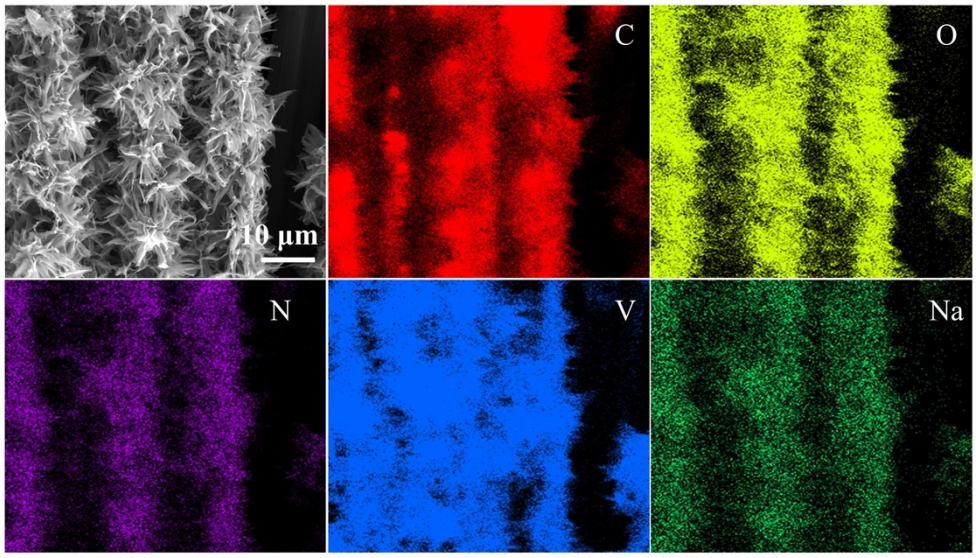

Fig. S16. EDS mappings of NaNVO@CC after 2000 cycles at 5.0 A g^{-1}.

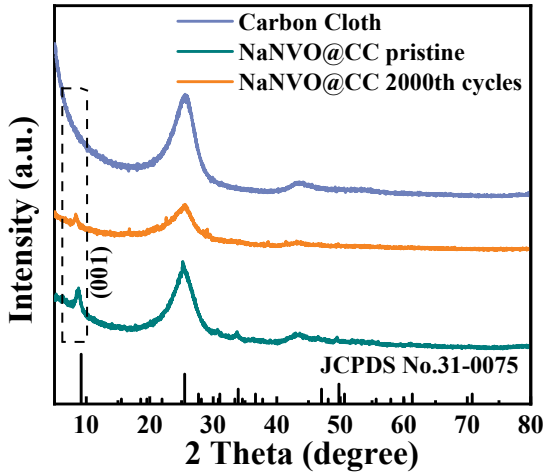

Fig. S17. XRD patterns of NaNVO@CC after 2000 cycles at 5.0 A g^{-1}.

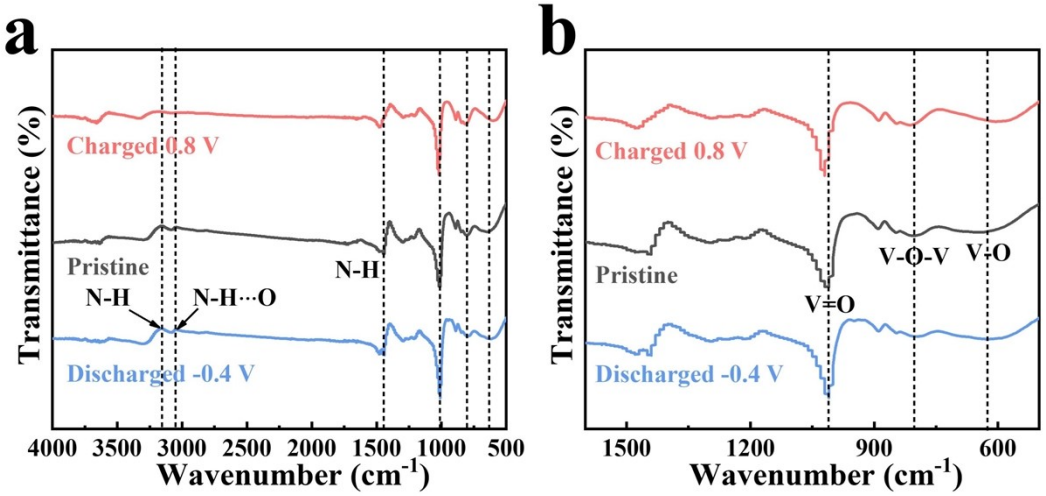

Fig. S18. (a, b) Ex-situ FTIR spectra of NaNVO@CC at various states (pristine, fully charged, and fully discharged).

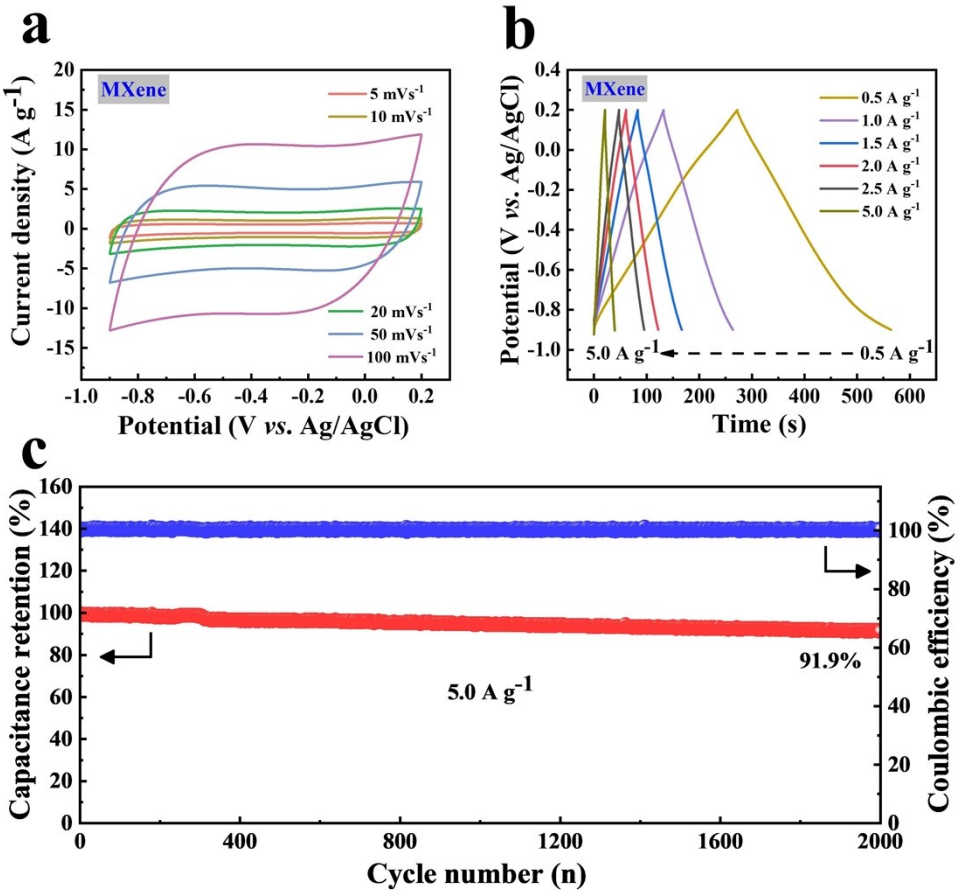

Fig. S19. (a) CV curves of $Ti_3C_2T_x$ MXene anode from 5.0 mV s^{-1} to 100 mV s^{-1}. (b) GCD curves of $Ti_3C_2T_x$ MXene anode from 0.50 A g^{-1} to 5.0 A g^{-1}. (c) Cycling life and coulomb efficiency of $Ti_3C_2T_x$ MXene anode at 5.0 A g^{-1}.

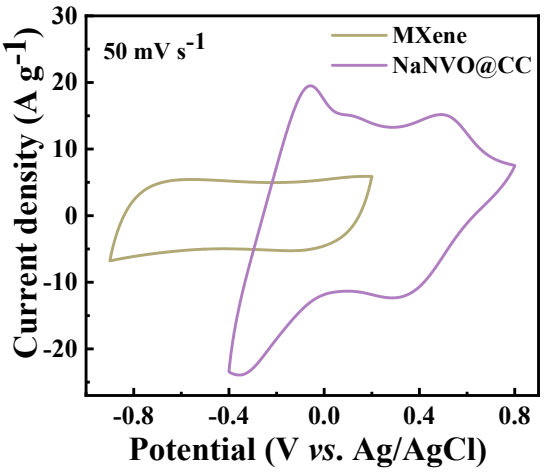

Fig. S20. The CV curves at 50 mV s^{-1} of NaNVO@CC cathode and $Ti_3C_2T_x$ MXene anode.

Table S3. Comparison of the capacitance, energy density and power density of NaNVO@CC//$Ti_3C_2T_x$ MXene with previously reported NH_4^+ energy storage devices.

Material	Electrolyte	Current density	Capacitance	Energy density (Wh kg^{-1})	Power density (W kg^{-1})	Ref.
NaNVO@CC// $Ti_3C_2T_x$ MXene	1.0 M $(NH_4)_2SO_4$	0.50 A g^{-1}	193 F g^{-1}	77.7	424.3	This work
VOH/PEDOT// AC	1.0 M PVA/NH_4Cl	1 mA cm^{-2}	328 F cm^{-2}	10.4	35.7	10
MnAl-LDH/ PTCDI	0.5 M $(NH_4)_2SO_4$	0.5 A g^{-1}	47 mAh g^{-1}	45.8	163.5	11
MC//MC	$(NH_4)_2SO_4$-gel	1 A g^{-1}	174 F g^{-1}	78.3	929.1	12
NVO//AC	1.0 M NH_4Cl/PVA	1 mA cm^{-2}	324 F cm^{-2}	9.16	15.9	9
PDI-Ph// ATA (BSH)	30 M NH_4Ac	0.2 A g^{-1}	42 mA h g^{-1}	16.5	719	13
ACC@VPP// PTCDI	1.0 M PVA/NH_4Cl	1 mA cm^{-2}	411 F cm^{-2}	10.6	28.9	5
h-MoO_3/ CuFe PBA	1.0 M NH_4Cl	1 A g^{-1}	42 mA h g^{-1}	21.3	277	6
MoS_2@PAN// MoS_2@PANI	1.0 M NH_4Cl	1 A g^{-1}	219.8 F g^{-1}	59.8	725	7
δ-MnO_2//ACC	1.0 M $(NH_4)_2SO_4$	2 mA cm^{-2}	1550 F cm^{-2}	861.2 μWh cm^{-2}	20 mW cm^{-2}	14
PVO// AC	1.0 M PVA/NH_4Cl	1 mA cm^{-2}	310 mF cm^{-2}	1.72 Wh m^{-2}	2.5 W m^{-2}	1

References

1 P. Wang, Y. Zhang, Z. Feng, Y. Liu and C. Meng, *J. Colloid Interface Sci.*, 2022, **606**, 1322-1332.

2 H. D. Zhang, Y. Tian, W. Wang, Z. L. Jian and W. Chen, *Angew. Chem. Int. Ed.*, 2022, **61**, 202204351.

3 S. F. Kuchena and Y. Wang, *Electrochim. Acta*, 2022, **425**, 140751.

4 Y. Song, Q. Pan, H. Lv, D. Yang, Z. M. Qin, M. Zhang, X. Sun and X. Liu, *Angew. Chem. Int. Ed.*, 2021, **60**, 5718-5722.

5 X. Chen, P. Wang, Z. Feng, C. Meng and Y. Zhang, *Chem. Eng. J.*, 2022, **445**, 136747.

6 G. Liang, Y. Wang, Z. Huang, F. Mo, X. Li, Q. Yang, D. Wang, H. Li, S. Chen and C. Zhi, *Adv. Mater.*, 2020, **32**, 1907802.

7 J. Dai, C. Yang, Y. Xu, X. Wang, S. Yang, D. Li, L. Luo, L. Xia, J. Li, X. Qi, A. Cabot and L. Dai, *Adv. Mater.*, 2023, **35**, 2303732.

8 X. Wu, Y. Qi, J. Hong, Z. Li, A. S. Hernandez and X. Ji, *Angew. Chem. Int. Ed.*, 2017, **56**, 13026-13030.

9 P. Wang, Y. Zhang, H. Jiang, X. Dong and C. Meng, *Chem. Eng. J.*, 2022, **427**, 131548.

10 X. Chen, P. Wang, Z. Feng, Y. Liu, M. Cui, C. Meng and Y. Zhang, *Advanced Sensor and Energy Materials*, 2022, **1**, 100013.

11 Q. Liu, F. Ye, K. Guan, Y. Yang, H. Dong, Y. Wu, Z. Tang and L. Hu, *Adv. Energy Mater.*, 2023, **13**, 2202908.

12 J. Dai, X. Qi, L. Xia, Q. Xue, L. Luo, X. Wang, C. Yang, D. Li, H. Xie, A. Cabot, L. Dai and Y. Xu, *Adv. Funct. Mater.*, 2023, **33**, 2212440.

13 K. C. S. Lakshmi, X. B. Ji, T. Y. Chen, B. Vedhanarayanan and T. W. Lin, *J. Power Sources*, 2021, **511**, 230434.

14 Q. Chen, J. Jin, M. Song, X. Zhang, H. Li, J. Zhang, G. Hou, Y. Tang, L. Mai and L. Zhou, *Adv. Mater.*, 2022, **34**, 2107992.